3D Thermal Analysis of Li-ion Battery Cells with Various Geometries and Cooling Conditions Using Abaqus

Kim Yeow, Ho Teng, Marina Thelliez, Eugene Tan

AVL Powertrain Engineering

Abstract: Modeling thermal behavior of Li-ion cells for vehicle electrification applications is a challenging task. AVL has developed 3D-FEA models to simulate the electro-thermal behavior of Li-ion battery cells with various geometries using Abaqus. In these models, the Li-ion battery system is simplified and modeled as heterogeneous solid medium consisting of a single or multiple equivalent battery layers with composite electrical and thermal conductivities for the equivalent anode, cathode and separator. Thermal behaviors of cylindrical, prismatic and pouch Li-ion battery cells and modules were analyzed under different electrical loads and cooling conditions. Simulation results were compared with available battery temperature measurements (covering cylindrical-cell and pouch-cell modules) and good agreements were observed. This indicates that the 3D electro-thermal model employed in this study characterizes the electro-thermal behavior of the Li-ion battery cells reasonably well.

Keywords: Lithium-ion battery, cells, modules, electro-thermal modeling, cooling

1. Introduction

Lithium-ion (Li-ion) batteries are widely selected as the energy storage devices for Hybrid Electrical Vehicles (HEV), Plug-in Hybrid Electrical Vehicles (PHEV), and Electrical Vehicles (EV) due largely to their high energy density, high power density, good stability and low charge loss when not in use. In a battery pack, the cells are assembled in groups or modules to obtain the required pack capacity, and modules are connected in series to provide the required pack voltage. For high-power battery packs such as those for HEV and PHEV applications, considerable amount of heat can be generated in the cells as a result of high discharge/regen pulse currents during duty cycles, causing rapid rise in cell temperature. For optimal performance of a battery pack, working temperatures of the cells in the pack should be controlled to within a proper range (ideally between 20 $^{\circ}$C to 40 $^{\circ}$C) and the temperature distribution in the cells should be as uniform as possible. The pack power capability is affected significantly by temperatures of the cells within the pack: in low temperature operations, the pack power capability is limited by the coolest cell; when operated at elevated temperature, the pack safety and thus the maximum allowed pack power are determined by the hottest cell. The maximum cell temperature and the maximum differential cell temperature are crucial factors to the cell safety and durability.

Figures 1 to 3 show the structures of cylindrical, prismatic and pouch Li-ion cells used in the battery packs for HEV, PHEV or EV applications. These three types of cells have advantages and disadvantages. Cylindrical cells (Figure 1) are easier to manufacture and have good mechanical stability and high energy density. However they have a low packing efficiency, resulting in a

relatively low energy density for the pack. Prismatic cells (Figure 2) typically have jelly roll or stacked electrodes, and they are mechanically robust and have a high packing efficiency. They have slightly lower energy density and are more expensive to manufacture compared to cylindrical cells. Pouch cells (Figure 3) have higher energy density than the other two designs. They are relatively inexpensive and provide design freedom on dimensions, which often makes the pouch cells the first choice in the cell selection for high capacity PHEV or EV packs. However, their disadvantages are: (1) mechanically vulnerable and thus requiring cell cartridges to hold them, (2) prone to swelling during operations especially when the cells age, and (3) has no mechanism for gas venting (as opposed to cylindrical and prismatic cells). Gas venting for the pouch cell involves swelling/breaking of the pouch and hence causing cell failure.

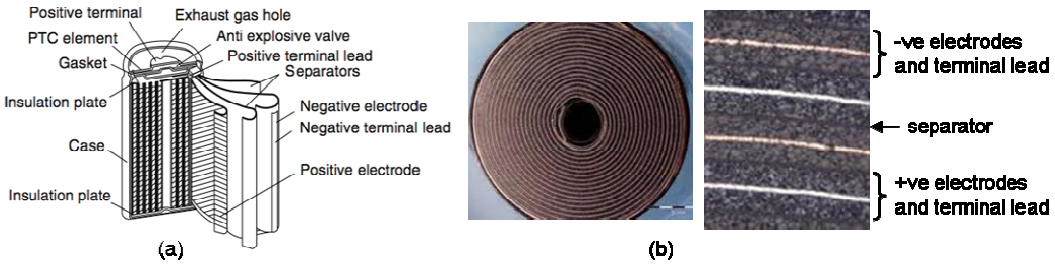

Figure 1. (a) Spiral wound structure for a cylindrical cell; (b) Sectional view of spiral wound core of a cylindrical cell and details of battery layers in the cell [1].

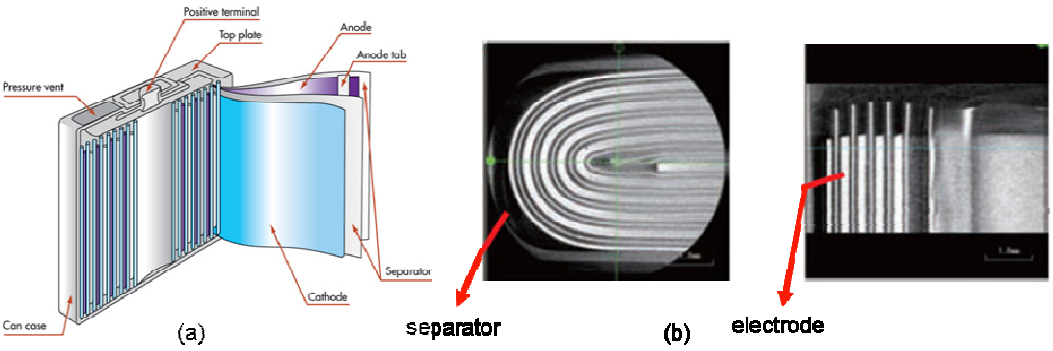

Figure 2. (a) Multi-folded-layer structure of a prismatic cell (b) Sectional view of X-ray pictures showing battery layers in the cell [2].

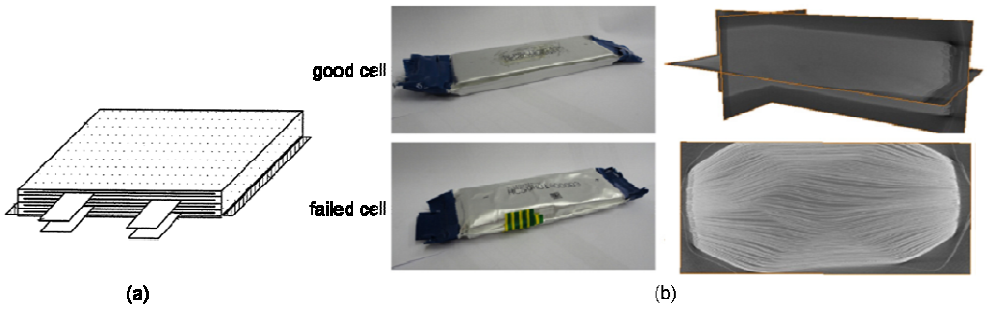

Figure 3. (a) Multi-stacked-layer structure of a pouch cell; (b) Sectional view (electronic magnification scanning) of the core of a pouch cell [3].

All the three types of Li-ion cells contain dozens of parallel thin battery layers whose dimensions are on the order of 10^2 microns [4,5]. Each of the battery layers in the cells consists of two electrodes (cathode and anode), a separator and two current collectors (copper for anode and aluminum for cathode). The electrodes and the separator are porous media filled with electrolyte as illustrated in Figure 4. During cell usage, the current flow (from one electrode to the other in each of the battery layers in the cell) involves electronic charge transfer through an external electrical circuit and ionic charge transfer through the internal path, i.e., the electrolyte [6]. Modeling the thermal behavior of the Li-ion cells for vehicle electrification applications is a challenging task. AVL has developed 3D electro-thermal models using the Finite Element Analysis (FEA) tool Abaqus [7] for simulating the electro-thermal behavior of Li-ion battery cells with various geometries. The 3D-FEA model and the simulation results for the various battery cells/modules will be discussed in the following sections of this paper.

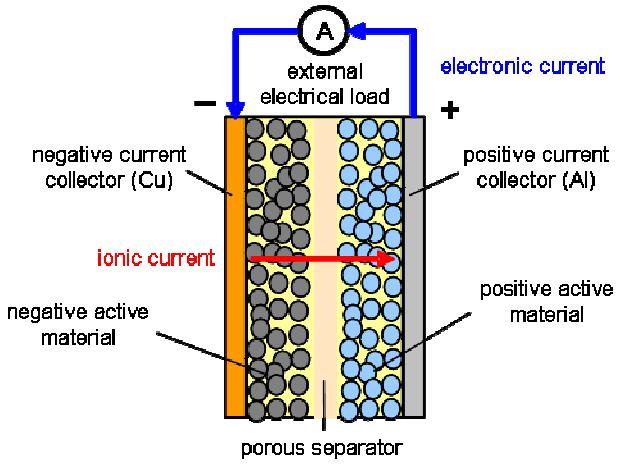

Figure 4. Illustration of the structure of a single battery layer in a Li-ion cell.

2. Modeling Approach

As aforementioned, a Li-ion battery cell has many parallel thin battery layers across its thickness. In an ideal design, the current flows in all of these battery layers are very similar. In a Li-ion battery cell, the ionic charge (the lithium ions) transfer from one electrode to the other takes place only through the electrolyte (Figure 4), i.e., the electro-chemical processes in the cell are confined in the space between the two electrodes in each of the thin battery layers with a dimension in the order of 10^2 microns. In contrast, the electronic charge (the electrons) transfer in each of the battery layers in the cell takes place along the entire current-collector surfaces whose dimensions are several orders of magnitude greater than that of the battery-layer thickness. Under a given cell terminal current, the current density distributions are similar in the current collectors as well as in the sources for the currents – the electrodes for all the battery layers. As indicated in Figure 4, the electrolyte in each battery layer is distributed in the pores of the electrodes and the separator. Dimensions for these pores are several orders of magnitude smaller than that of the thickness of a single battery layer.

For a cell under a discharge process with a current I, the dissipation of chemical energy into heat in the cell can be characterized by the difference between the open circuit voltage of the cell E_0 (the best voltage that the cell can provide at a given state of charge and temperature for a given cell chemistry) and the terminal voltage V as

$$V = E_0 - (\Delta V_1 + \Delta V_2 + \Delta V_3) \qquad (1)$$

where ΔV_1, ΔV_2 and ΔV_3 represent the three major voltage losses due respectively to: (1) the ohmic resistance of the electrodes and current collectors, (2) the activation polarization at the electrode-electrolyte interfaces, and (3) the concentration polarization as a result of the unbalanced transient electronic current in the electrodes and ionic current in the electrolyte. ΔV_1 is related to the electronic current, and ΔV_2 and ΔV_3 are due largely to the ionic current resistances in the electrolyte. For a given State of Charge (SOC) and temperature (T), Figure 5 illustrates the E_0-V relationship at different cell currents. All three voltage losses increase with increasing cell current with the polarization resistances dominate the overall resistance at high cell currents as illustrated in Figure 5.

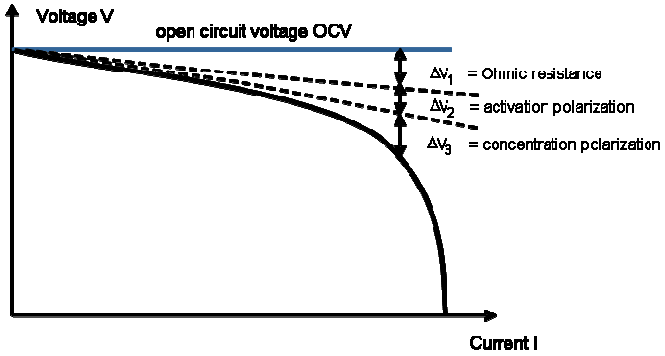

Figure 5. Voltage losses due to various resistances under different cell currents.

The cell heat generation Q resulting from cell chemical energy dissipation can be described by the product of the cell current and the voltage drop due to the chemical energy dissipation as

$$Q = I \times (E_0 - V) \qquad (2)$$

Alternatively Equation 2 may be expressed as

$$Q = I^2 \times R_i \qquad (3)$$

where $R_i = (E_0 - V)/I$ is the cell internal resistance. For battery cells in HEV and PHEV applications, R_i is commonly determined with the Hybrid Pulse Power Characterization (HPPC) current I_{HPPC}, which can be defined based on the target pack load [8]. USDOE [8,9] and USCAR / USABC [10] recommend that R_i be evaluated with a 10-second pulse HPPC current, for which contributions are included of the resistances to electrical and ionic charge transfers. The internal resistance so-determined is only a function of State of Charge (SOC) and temperature (T). Figure 6 shows a R_i-DOD-T map for a reference Li-ion cell, where DOD (= 1 – SOC) is the Depth of Discharge. As illustrated in Figure 6, the cell internal resistance increases with decreasing cell temperature and increasing depth of discharge.

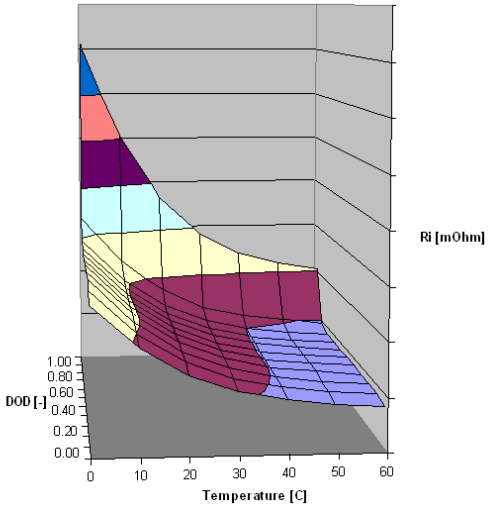

Figure 6. Internal resistance of a Li-ion cell with temperature and DOD.

The internal resistance determined from the HPPC tests is a bulk property for a battery cell. In the thermal analysis of a cell, it is not practical or necessary to model the details of the dozens of thin porous battery layers in the cell. If the cell heat generation can be estimated from the cell performance data, then based on the characteristics of the current density distributions in the current collectors and electrodes in the battery layers, the cell may be simplified to contain just one or several equivalent battery layers and modeled as a continuous heterogeneous solid medium,

in which heat conduction takes place [11,12]. Changes in the cell temperature due to the cell usage can thus be characterized with energy balance on a unit cell volume as

$$\rho C_p \frac{\partial T}{\partial t} = \nabla \cdot (k \nabla T) + q \qquad (4)$$

where ρ, C_p and k are the local density, heat capacity and thermal conductivity of the cell medium, T is the temperature, t is the time and q is the heat generated. Because of the layered structure, thermal behavior of the cell should be characterized with the effective thermal properties. Each of the battery layers with the same thermal properties may be treated as a component of the heterogeneous solid medium. The composite local volumetric heat capacity may be expressed as

$$\rho C_p = \frac{\sum_i \rho_i C_{p,i} V_i}{\sum_i V_i} \qquad (5)$$

where the subscript i indicates the properties for the component i and V is volume. Thermal conductivities at the component interfaces should be determined based on connections of the components. For series connections, the composite thermal conductivity is given as

$$k = \frac{\sum_i L_i}{\sum_i (L_i / k_i)} \qquad (6)$$

For parallel connections, the expression for the composite thermal conductivity becomes

$$k = \frac{\sum_i L_i k_i}{\sum_i L_i} \qquad (7)$$

In Equations 6 and 7, L_i and k_i are the thickness and the thermal conductivity for the component i respectively. Similarly, the composite electrical conductivities can also be expressed by Equations 6 and 7 in characterizing the electrical field of the cell. For a given cell with properly defined boundary conditions for heat transfer, Equation 4 can be solved using FEA approach. In this study, the electro-thermal behavior of the Li-ion battery cells and modules will be characterized using 3D-FEA model developed at AVL.

The approach of the cell modeling used in AVL battery electro-thermal model is illustrated in Figures 7 and 8. Figure 7 shows the coupling of governing equations characterizing the electrical field and the temperature field of the cell. The cell electrical behavior is characterized with Poisson equation for the cell voltage potential, which may be understood as Ohm's law in a differential form. The Ohm's law equation and the Fourier equation characterizing the thermal behavior of the cell are coupled through the current density under a given cell terminal current. Figure 8 shows the procedure of characterizing the electro-thermal behavior of the cell. For a given cell, its electrical behavior is characterized with the cell voltage potential V = V(DOD,A,T) and the cell internal resistance $R_i = R_i$(DOD,B,T), where A and B are parameters related to the cell chemistry. Because the Ohm's law equation does not contain time, the modeling of the electrical field of the cell in a discharge process involves the processes of initialization, localization of the bulk cell properties obtained from the cell performance data, and continuous update of the local parameters governing the local SOC (or DOD) and local internal resistance during the cell

discharge or charge. The spatial and temporal characterizations of the electrical field of the cell are carried out by two user subroutines. Due to the coupling of the electrical field and the temperature field, variations of the electrical field of the cell also induce changes in the cell temperature distribution.

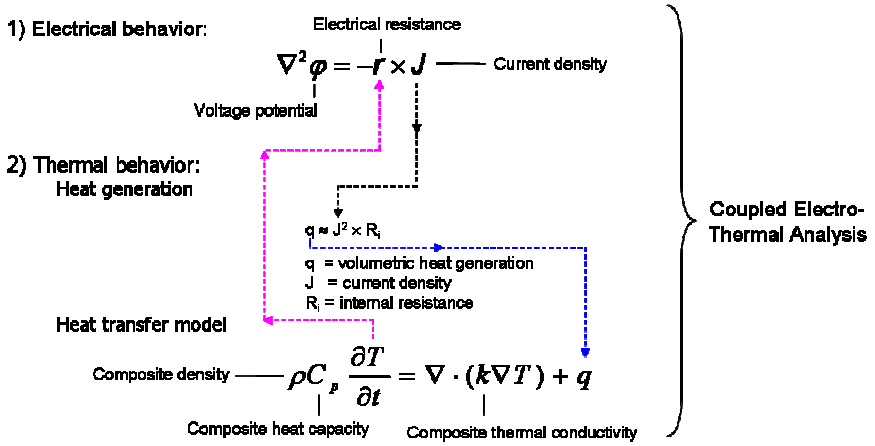

Figure 7. Coupling of electrical field with temperature field of the cell.

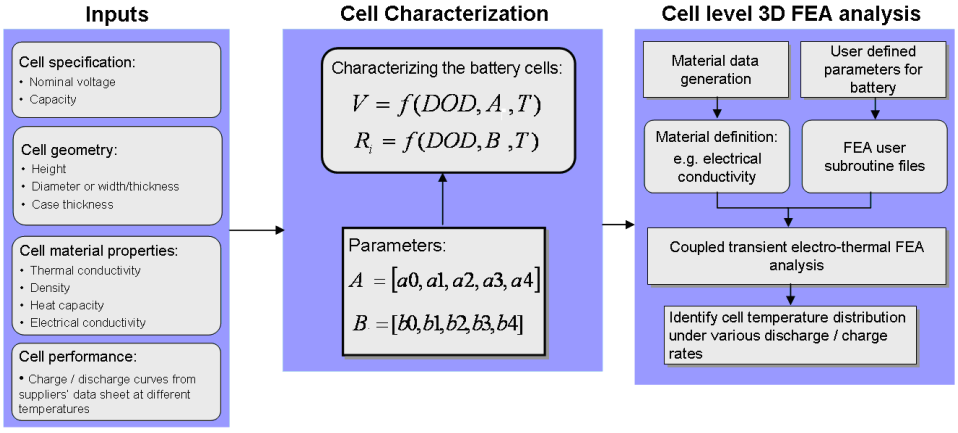

Figure 8. Procedure for characterizing electro-thermal behavior of the cell.

3. Battery cell modeling

In this section, the focus is on techniques in modeling for cells with different geometries. For simplicity, direct air cooling is assumed for all the cells. Validation of the model predictions with

the available test data will be discussed in the next section where the focus is on the cooling of the battery module. All battery cells studied in this paper are Li-ion battery cells.

3.1 Pouch Cell

In pouch cells the temperature gradient across the cell thickness is generally small and negligible in comparison to those in the other two dimensions. Hence, pouch cells can be modeled with only one equivalent battery layer. Figure 9a shows a simplified model for a pouch cell. The model includes the current collecting tabs and equivalent electrodes. Details in modeling techniques for a pouch cell can be found in the authors' previous work [11]. Figure 9b shows the selected simulation results for two pouch cells: an 8Ah cell (dimensions = 142mm × 115mm × 8.5mm) with the positive and negative terminal tabs arranged on the opposite sides of the cell and a 5Ah cell (dimensions = 190mm × 108mm × 7mm) with the two terminal tabs arranged on the same side. The cells are air cooled with Heat Transfer Coefficient (HTC) corresponding to that in channel flows. The simulated results represent cell temperatures at 80% DOD in a discharge process from a fully charged state (DOD = 0) under 13.5C rate for the 8Ah cell and 11C rate for the 5Ah cell. It is seen that the cell temperature distributions for pouch cells are influenced greatly by terminal tab designs.

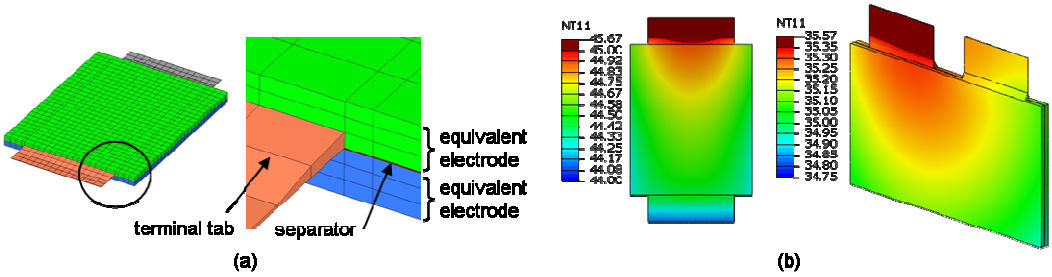

Figure 9. (a) Simplified FEA model for pouch cell; (b) Simulation results.

3.2 Prismatic Cell

Prismatic cells are generally enclosed in a metal case. The thickness of a prismatic cell is not too much smaller than the cell length and height. Thus, the cell may be modeled with multiple equivalent battery layers in order to better simulate the maximum differential temperature across the cell thickness. Figure 10a shows the simplified model for a 6Ah prismatic cell (dimensions = 112mm × 70mm × 27mm). The model includes a metal case, two terminal poles, current collecting tabs and equivalent electrodes for three equivalent battery layers. The cell is air cooled with HTC corresponding to that in a channel flow. Figure 10b shows the selected simulation results for both cell surface and core temperatures at 80% DOD in a discharge process from a fully charged state (DOD = 0) under 10C rate. The three-layer model predicts that the maximum cell temperature is in the center of the cell for this prismatic cell and the cap of the cell case has the lowest temperature since it has no direct contact with the cell.

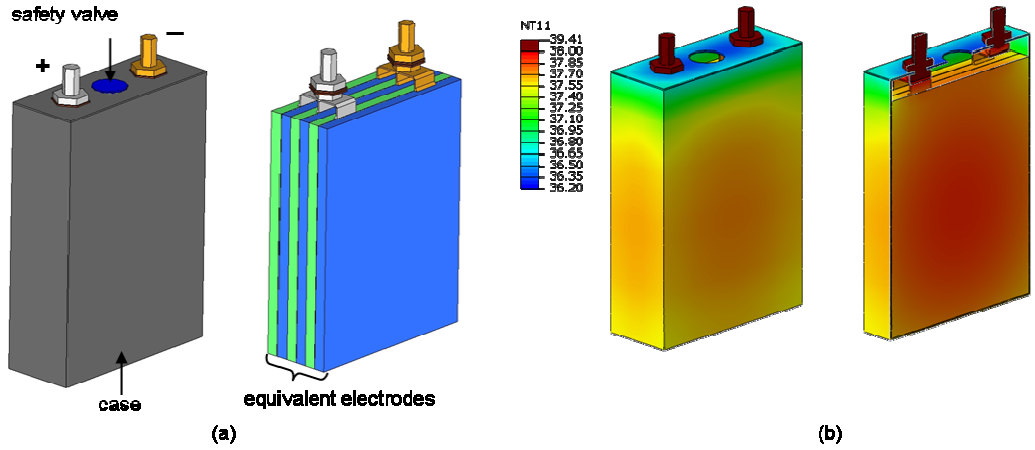

Figure 10. (a) Simplified FEA model for prismatic cell; (b) Simulation results.

3.3 Cylindrical Cell

All cylindrical cells have metal cases and the cell terminals are generally arranged on opposite ends of the cell. Due to the spiral wound structure, the surface area of a battery layer varies with the radius of the layer position. Hence the number of current collection tabs also varies with the surface area of the battery layer in the cell [13]. Several methods have been proposed to model the spiral wound structure of the cylindrical cell [14-17]. The techniques developed previously for modeling cylindrical cells have been reviewed by the authors of this study [11]. Figure 11 shows the simplified models for a 2.3Ah cylindrical cell (diameter = 26mm; height = 65 mm): (a) one-equivalent-layer model and (b) three-equivalent-layer model.

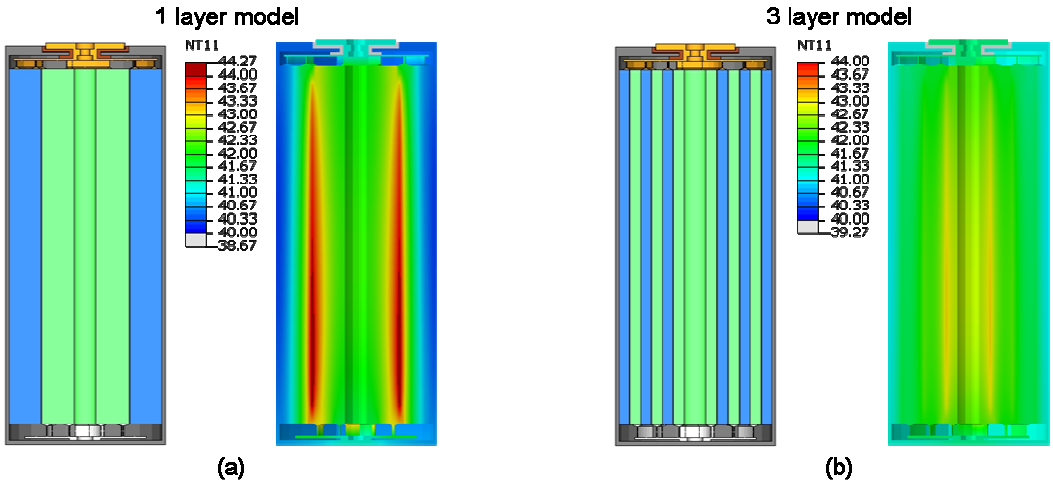

Figure 11. (a) One-equivalent-layer model; (b) Three-equivalent-layer model.

Each equivalent battery layer has three concentric rings: the inner ring is an equivalent cathode with a positive current collector connecting it with the positive terminal of the cell; the outer ring is an equivalent anode with a negative current collector connecting it with the negative terminal of the cell; the middle ring represents the separator. The cell is assumed to be cooled under natural convection with 25 °C ambient air and HTC = 10 W/m^2-°C. The selected simulation results for cell temperatures at 90% DOD in a discharge process from a fully charged state (DOD = 0) under 10C rate are also presented in Figure 11. It is seen that the maximum cell temperature predicted by the three-equivalent-layer model is about 1 °C lower than that predicted by the one-equivalent-layer model under the specified heat generation and cooling conditions. This is because the cell heat distribution is more uniform in the three-equivalent-layer model than in the one-equivalent-layer model. It is also apparent that the maximum-cell-temperature location shifts to the inner adiabatic surface of the cell as the number of the equivalent battery layers in the model increases.

4. Battery module modeling

4.1 Battery module with indirect liquid cooling

Figure 12 shows a three-cell module with indirect liquid cooling. In the module, three 80Ah pouch cells (dimensions = 240mm × 260mm × 11.5mm) are arranged in series electrically with their terminal tabs connected with busbars. Each cell in the module is cooled via a 1.5-mm thick aluminum cooling fin which is in contact with a cold plate located on the opposite side of the cell terminal tabs. The side surface of the cell that is not in contact with the cooling fin is thermally insulated from the next cooling fin by an elastomeric thermal pad. The cells were modeled with a one-equivalent-layer model as illustrated in Figure 12.

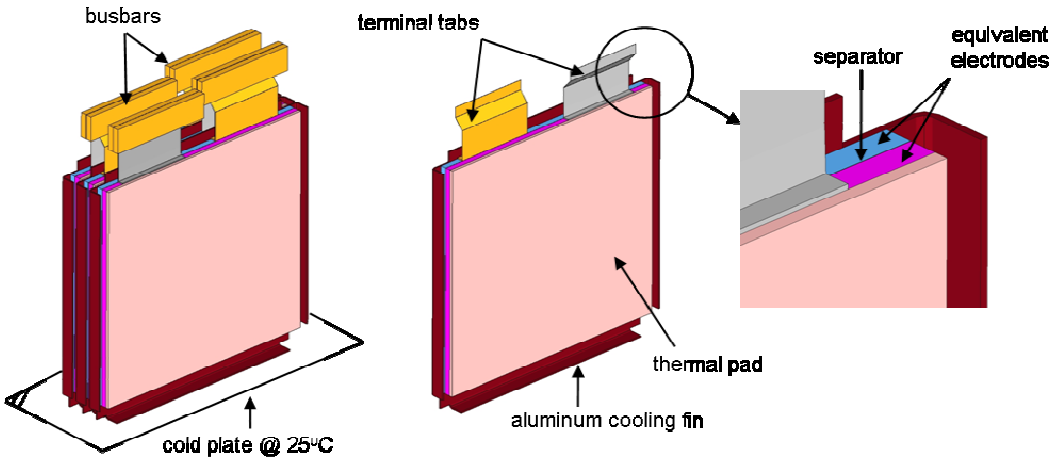

Figure 12. FEA model for three pouch cell module with indirect liquid cooling.

Figure 13 compares the measured and simulated temperatures at 90% DOD in a discharge process from a fully charged state (DOD = 0) under 2C rate. During the test, the cold plate surface temperature was maintained at 25 °C. Because the terminal tab and busbar temperatures were not measured, only the cell temperatures are compared. Since the three cells in the module are thermally symmetric, only the results for the middle cell in the module are presented. The measured cell temperatures are presented in a contour plot with 0.5 °C as the interval between two contour lines. It is seen that the simulated cell temperatures correlate reasonably well with the measurements both in the maximum cell temperature and the cell temperature distribution. This indicates that the model can reasonably characterize the thermal behavior of the cells in the module.

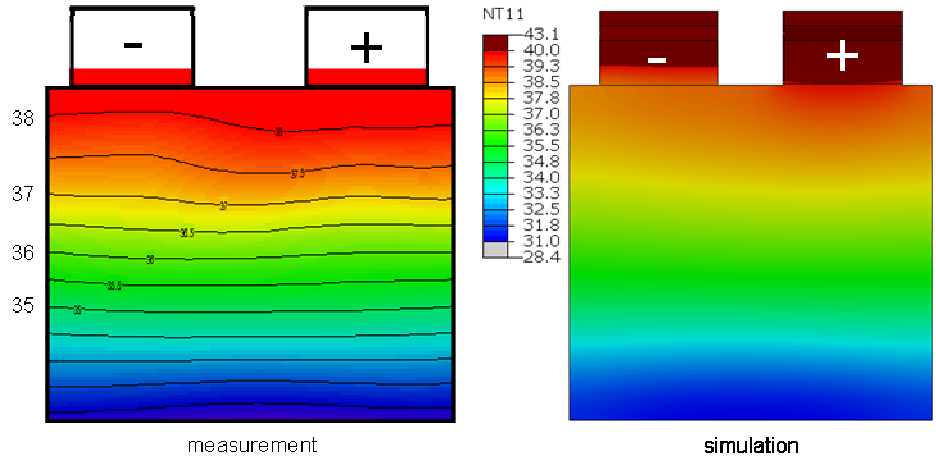

Figure 13. Comparison of measured and simulated cell temperatures.

4.2 Battery module with direct air cooling

Figure 14a shows the FEA model for a module assembled with 44 A123-ANR26650M1A cylindrical cells (diameter = 26 mm; height = 65 mm) with direct air cooling. The module has an 11P4S configuration, i.e., the 44 2.3Ah cells are arranged in 4 groups that are connected in series. The 11 cells in each of the groups are connected in parallel. The module was taken from an A123 Hymotion™ L5 PCM battery pack consisting of 14 identical modules connected in series [18,19]. For simplicity, the one-equivalent-layer model discussed in Section 3.3 was used to characterize the electro-thermal behavior of the cells in the module. In order to obtain more accurate thermal boundary conditions for the cells in the module, 3D Computational Fluid Dynamic (CFD) simulations on the air flow distribution in the module were performed using AVL FIRE [20]. Several analysis iterations were performed between FEA and CFD where the wall temperature (as boundary condition for CFD analysis), the HTC and the air temperature (as boundary condition for the FEA analysis) were updated in successive iterations. More detailed discussion regarding the CFD simulations on the air flow distribution in the module were reported in a previous paper by

the authors [11]. The sectional view in Figure 14b shows the simulated module temperatures at 90% DOD in a discharge process from a fully charged state (DOD = 0) under 5C rate. Figure 15 compares the simulated cell temperatures with the measurements under 5C discharge rate for three selected cells: cell A at the module entrance and cells B and C at the module exit with B at the center and C on the side. Overall, the simulated cell temperatures and the measurements agree reasonably well. The relatively poor prediction for cell B was due to the influence of the air leakage through the two bolt holes along the centerline of the module in the test, which generated additional cooling over the busbar surfaces. The busbar surface cooling was not considered in the simulation.

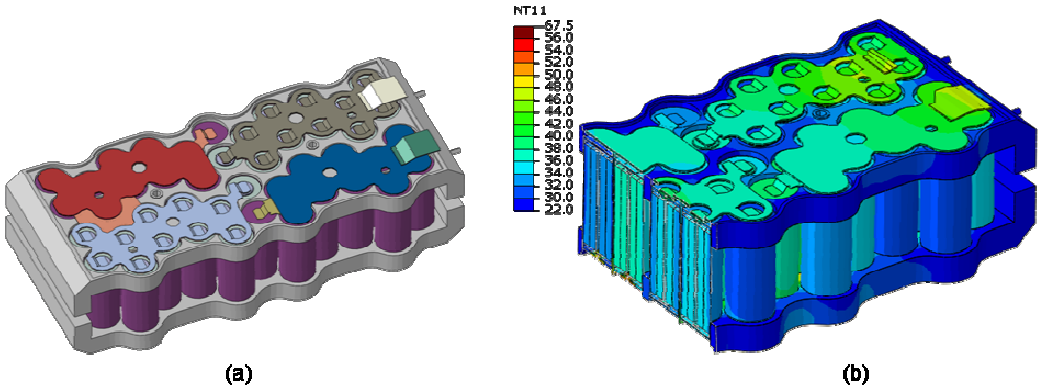

Figure 14. (a) FEA model for the 44 cylindrical-cell module; (b) Simulation result.

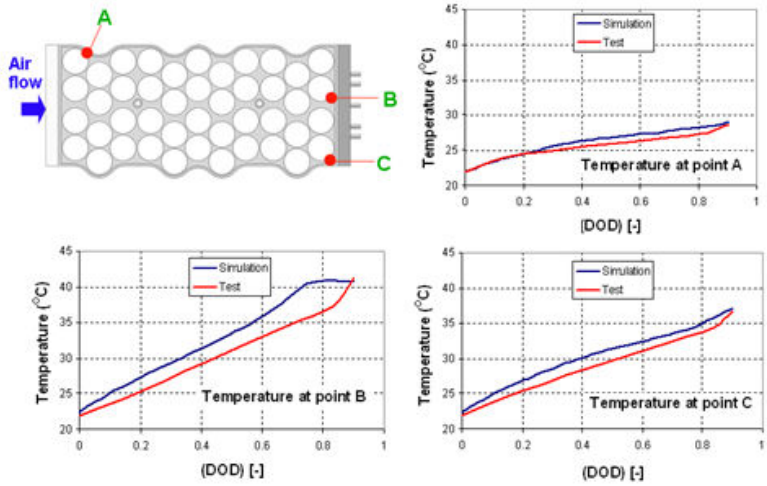

Figure 15. Comparison of the simulated and measured cell temperatures.

4.3 Battery modules with indirect air cooling and heating

4.3.1 Cooling analysis

Figure 16 shows the FEA models for two pouch-cell modules with indirect air cooling. The two modules are different only in the structures of the air cooling channels: one without fin inserts (Figure 16a) and the other with fin inserts (Figure 16b). Both modules are stacked with twelve 8Ah pouch cells (dimensions = 140mm × 190mm × 8.5mm) connected in series. The cells are cooled indirectly through six 1-mm thick aluminum cooling plates sandwiched between each pair of cells. Each of the cooling plates has an extended cooling fin exposed in the air flow channel. In the space between each pair of cells without a cooling plate, a 1-mm thick elastomeric thermal pad is inserted. For a better view of the cooling units in the module, the module frame and electrical connectors are removed from the display. The section of the cooling plate through the module plastic frame and the fin section of the cooling plate (where air cooling takes place) is each 19 mm wide. The cooling-plate pitch (i.e., the space for air flow between the two cooling plates) is also 19 mm. Because the length of the air cooling channel is hydraulically short (channel-length/plate-pitch < 10), some cooling air in the center of the channel may not be effectively involved in cooling of the plate (i.e. short circuited). To improve the effectiveness of air utilization, a model with fin inserts placed in spaces between the cooling plates (Figure 16b) is also evaluated. The fin inserts have an equivalent fin density of 12 fins/in, with a total of 10 fins inserted in the 19 mm space between the cooling plates.

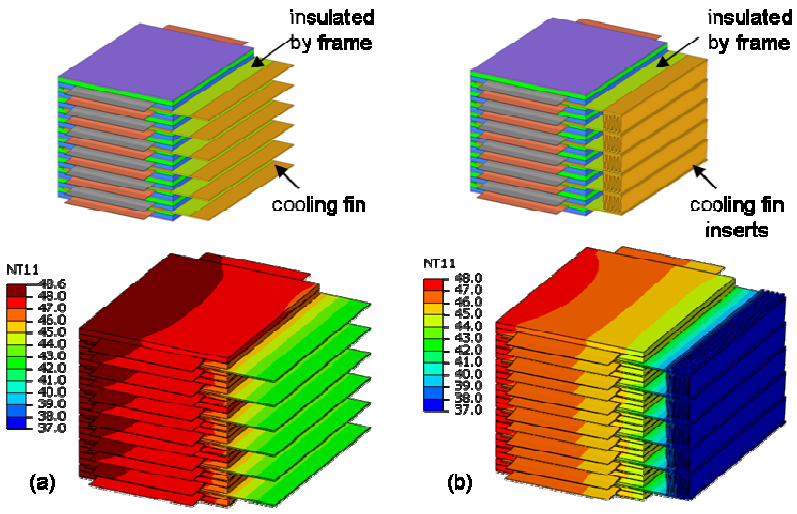

Figure 16. FEA models for 12-pouch-cell modules and simulation results: (a) without fin inserts in air channel; (b) with fin inserts in air channel.

Thermal behavior for both modules was evaluated under 5C discharge rate from the fully charged condition (DOD = 0) to 80% DOD. Boundary conditions for heat transfer in the air flow channels are T_{air} = 35 °C and HTC = 60 W/m^2-°C (corresponding to channel flow). The simulation results plotted to the same scale are also presented in Figure 16. As seen in Figure 16, temperatures of the fin inserts are close to the air temperature, suggesting that the fin inserts improve the air utilization considerably. Figure 17 plots the temperature distributions along the center lines of the cooling plate in the middle of the module for the two models. The followings are apparent: (1) the temperatures of the fin inserts are close to the air temperature, suggesting that the fin inserts improve the air utilization and heat transfer effectiveness considerably, and (2) the temperature distribution among cooling plates is influenced significantly with changes in heat transfer on cooling-fin surfaces.

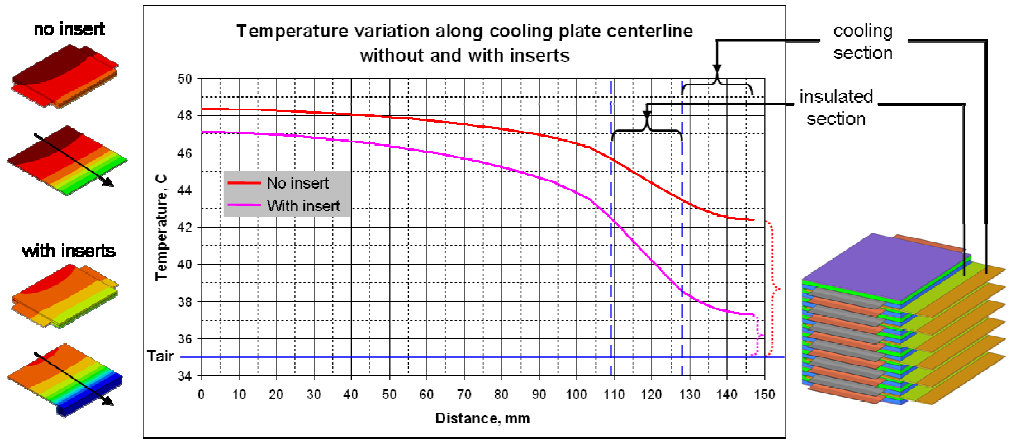

Figure 17. Temperature variations along centerline of cooling plate at DOD = 80%.

4.3.2 Heating analysis

The same two battery modules as outlined and shown in Figure 16 were used in the warm-up analysis. In this case it is assumed that the battery pack is thermally soaked in -20 °C environment. The module is discharged under a constant 1C rate to provide electrical power to the heater. Hot air boundary condition of T_{air} = 40 °C and HTC = 60 W/m^2-°C are applied to the air flow channels for the pack warm-up. The pack is fully functional only after the minimum cell temperature becomes ≥ 0 °C. The time it takes for the cell temperature to reach 0 °C was hence used as a criterion for comparing the effectiveness of the two cooling fin designs. Because of the small temperature difference between the cell and the cooling plate as previously observed, the cell warm-up is evaluated based on changes in the temperature of the aluminum plates.

Figure 18 shows temperatures in the modules (plotted to the same scale) without and with fin inserts in the air channels at the time when the minimum plate temperature reaches 0 °C at the adiabatic end. Figure 19 shows the transient temperatures at the adiabatic end of the aluminum

plate during the heating process. The simulation results indicate that the fin inserts improve the heating efficiency significantly. Without and with fin inserts, it takes 820 seconds and 480 seconds respectively for the adiabatic end of the aluminum plates to reach 0 ^{o}C. With the fin inserts, the warm-up time is 340 seconds shorter. The shorter the warm-up time, the lower the energy required for the pack warm-up. It also means that the battery pack can be fully functional that much sooner.

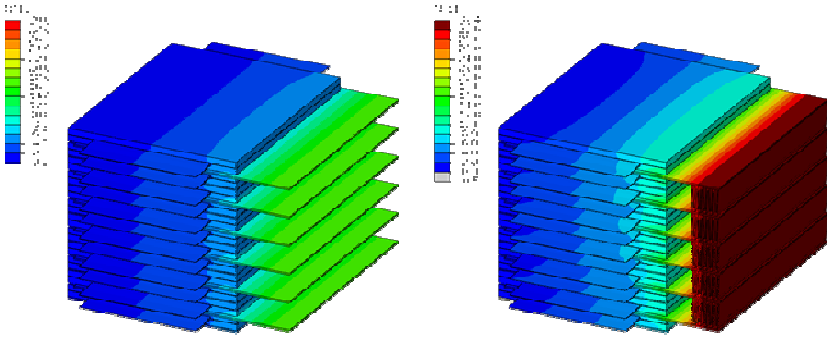

Figure 18. Results of heating simulation at the time the adiabatic edge reaches 0^{o}C for module without and with fin inserts.

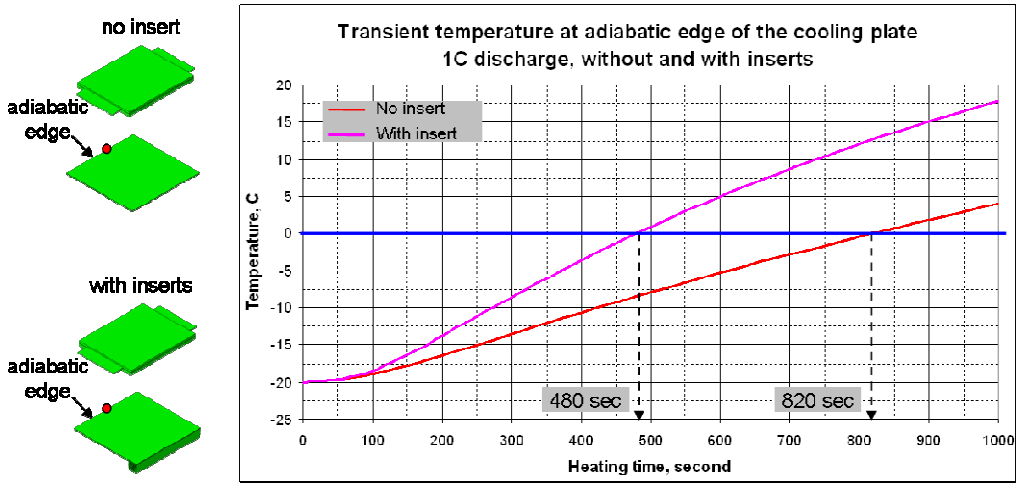

Figure 19. Transient temperature at the adiabatic edge of the cooling plate during warm-up.

Figure 20 shows the heat flux to each cell together with the internal heat generated during the heating process. The results show the effectiveness of the fin inserts in extracting energy from the heating air. It also shows that cell self heating contributed a small percentage of the overall heat during the cell heating process.

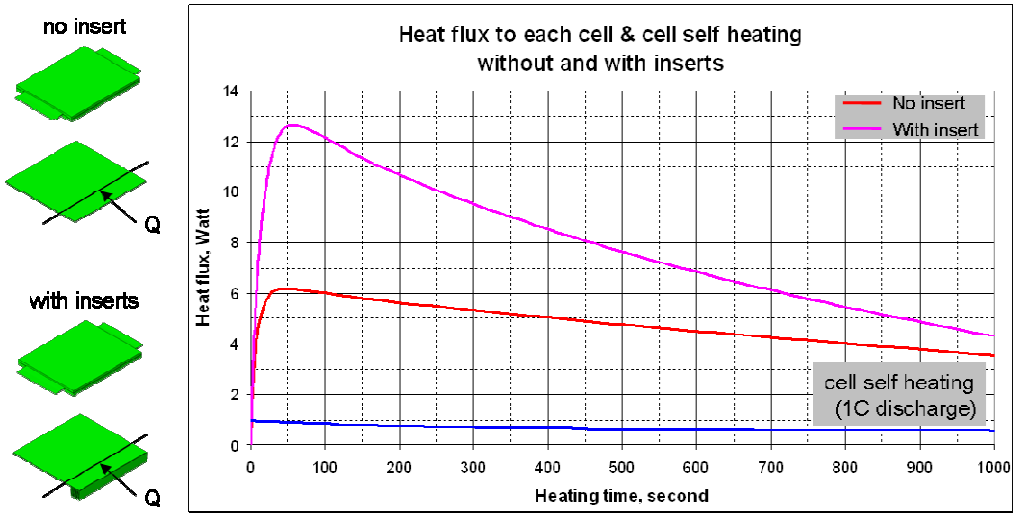

Figure 20. Heat flux to each cell and cell self heating during warm up.

5. Summary

AVL has developed a method to characterize the electro-thermal behaviors of Li-ion battery cells. 3D FEA models were used to analyze the thermal behavior of commercially available cylindrical, prismatic and pouch battery cells. Characteristics of these three types of cells may be summarized as follows. (1) Pouch cells have negligible temperature difference across their thicknesses. However they can have large differential cell temperatures across their cell surfaces in high current applications. For this type of cells, maximum cell temperatures are typically near the terminal tabs where local heat fluxes are high due to high local current densities. (2) For cylindrical cells, cell core temperatures can be significantly different from cell surface temperatures. This is because of the adiabatic condition at the cell core and decreasing heat transfer resistance with increasing radius. (3) For prismatic cells, differential temperature across the cell thickness must be considered. However, large thermal mass for this type of cell may mitigate the cell temperature rise. It is found that for cased cells (cylindrical and prismatic cells) the maximum cell temperature is in the core of the cell, not near the cell terminals as observed for the pouch cells. Simulation results were compared with available test data for battery temperature measurements covering pouch-cell and cylindrical-cell modules under different cooling conditions. Good agreement between the simulations and measurements were observed, indicating that the 3D electro-thermal model employed in this study reasonably characterizes the electro-thermal behavior of the Li-ion battery cells.

6. References

1. http://www.exponent.com/batteries_energy_storage_tech_2/.
2. http://www.ssi.shimadzu.com/markets/literature/C10GE021.pdf.
3. Yufit, V., Shearing, P., Hamilton, R.W., Lee, P.D., Wua, M. and Brandon, N.P., "Investigation of Lithium-ion Polymer Battery Cell Failure Using X-Ray Computed Tomography," Electrochem. Commun., Vol.13, pp.608-610, 2011.
4. Linden, D. and Reddy, T.B., Handbook of Batteries, 3rd ed., McGraw-Hill, 2002.
5. Brodd, R.J., "Lithium-Ion Cell Production Processes," Chapter 9, Advances in Lithium-Ion Batteries, W.A. Van Schalkwijk and B. Scrosati (ed.), Kluwer Academic / Plenum Publishers, 2002.
6. Thomas, K.E., Newman, J. and Darling, R.M., "Mathematical Modeling of Lithium Batteries," Chapter 12 in Advances in Lithium-Ion Batteries, Van Schalkwijk, W.A. and Scrosati, B. (ed.), Kluwer Academic / Plenum Publishers, 2002.
7. Simulia, Abaqus/Standard documentation, www.simulia.com/support/documentation.html.
8. Idaho National Engineering & Environmental Laboratory, PNGV Battery Test Manual, DOE/ID-10597, 2001.
9. Idaho National Engineering & Environmental Laboratory, Battery Test Manual for Plug-In Hybrid Electric Vehicles, INL/EXT-07-12536, 2010.
10. USCAR, USABC Manuals, available online via http://www.uscar.org/guest/tlc/3/Energy-Storage-TLC.
11. Ma, Y., Teng, H. and Thelliez, M., "Electro-Thermal Modeling of a Lithium-ion Battery System," SAE Paper No. 2010-01-2204, 2010.
12. Ma, Y. and Teng, H., "Comparative Study of Thermal Characteristics of Lithium-ion Batteries for Vehicle Applications," SAE Paper No.2011-01-0668, 2011.
13. Chu, A.C., Gozdz, A.S., Riley, G.N. and Hoff, C.M., "Battery Cell Design and Method of Its Construction," U.S. Patent 2007/0269685 A1, November 22, 2007.
14. Inui, Y. Kobayashi, Y. Watanabe, Y. Watase, Y. Kitamura, "Simulation of Temperature Distribution in Cylindrical and Prismatic Lithium Ion Secondary Batteries," Energy Conversion and Management, Vol.48, pp.2103-2109, 2007.
15. S. Al-Hallaj, H. Maleki, J. S. Hong, J.R. Selman, "Thermal Modeling and Design Considerations of Lithium-ion Batteries," J. Power Sources, Vol.83, 1 (1999).
16. T. D. Hatchard, D. D. MacNeil, A. Basu, J. R. Dahn, "Thermal Model of Cylindrical and Prismatic Li-ion Cells," J. Electrochem. Soc., Vol.148, 7, 2001.
17. T. I. Evans, R. E. White, " A Thermal Analysis of a Spirally Wound Battery Using a Simple Mathematical Model," J. Electrochem. Soc., Vol.136, 2145, 1989.
18. Iu, H.Y. and Smart, J., "Determining PHEV Performance Potential – User and Environmental Influences on A123 Systems' Hymotion™ Plug-In Conversion Module for the Toyota Prius," EVS24 International Battery, Hybrid and Fuel Cell Electric Vehicle Symposium, Stavanger, Norway, May 13-16, 2009.
19. http://www.a123systems.com/a123/products.
20. AVL GmbH, AVL-FIRE, Theory, Version 2009, AVL, Graz, 2009.